Normal-sense shear zones in the core of the Higher Himalayan Crystallines (Bhutan Himalaya): evidence for extrusion?

R. CAROSI[1,4], C. MONTOMOLI[1,4], D. RUBATTO[2] & D. VISONÀ[3,4]

[1]*Dipartimento di Scienze della Terra, via S. Maria 53, 56126 Pisa, Italy (e-mail: carosi@dst.unipi.it)*

[2]*Department of Earth and Marine Sciences – DEMS-Building 47, Daley Road, Australian National University, Canberra, Australia*

[3]*Dipartimento Mineralogia e Petrologia, corso Garibaldi 37, 35122 Padova, Italy*

[4]*Istituto di Geoscienze e Georisorse, CNR, via Moruzzi 1, 56100 Pisa, Italy*

Abstract: Recent fieldwork in western Bhutan, dedicated to unravelling the tectonic structure of the mid-crustal rocks, indicates a complex deformation pattern in the Greater Himalayan Slab (GHS). A system of normal shear zones, striking NE–SW and steeply to moderately dipping to the SE, has been recognized within this extruding slab or wedge of crystalline rocks. The zones are characterized by well developed shear-sense indicators pointing to a top-down-to-SE sense of shear. The main Barrovian metamorphic minerals are bent and stretched by extensional shear bands and associated deformation mechanisms indicate a range of brittle–ductile deformation conditions. Normal shear zones are concentrated in the middle–upper part of the GHS and indicate a thrust-transport-parallel lengthening of the core itself. Vorticity analysis highlights a non-coaxial flow with pure and simple shear acting together during deformation (mean vorticity number bracketed between 0.63 and 0.76). These data, when compared to available data near the tectonic boundaries of the GHS, indicate an increasing component of pure shear towards the interior of the GHS. The ages of zircon overgrowths and monazites from a slightly deformed granite, 20.5 $\pm$ 0.5 Ma, and a mylonitic granite deformed into the shear zones, 17.0 $\pm$ 0.2 Ma, bracket the age of shear zone formation at close to 17 Ma. According to our data, the normal shear zones could well accommodate the pure shear component of deformation localized in the inner part of the extruding wedge/slab and is compatible with a channel flow model.

The Himalayan orogen is regarded as one of the best examples of a collisional mountain belt in which contractional structures, such as thrusts and folds, have produced thickening of the continental lithosphere (Gansser 1964; Le Fort 1975). In the last two decades the Himalaya has attracted great attention among researchers since the recognition of apparent extensional structures along the top of the metamorphic core to this orogen (South Tibetan Detachment System (STDS); Caby *et al.* 1983; Burg *et al.* 1984; Herren 1987; Searle *et al.* 1988; Burchfiel *et al.* 1992) contemporaneous with contraction along its base (Main Central Thrust (MCT); Gansser 1964; Le Fort 1975). This striking geological feature led to the development of several models for extrusion of the slab- or wedge-shaped metamorphic core (Burchfiel *et al.* 1992; Hodges *et al.* 1992; Grujic *et al.* 1996, 2002; Grasemann *et al.* 1999; Vannay & Grasemann 2001; Law *et al.* 2004). These models have influenced our understanding of the tectonic and metamorphic evolution of the Himalayan belt, and have arguably helped to better clarify the evolution of other ancient (e.g. Urals (Chemenda *et al.* 1997; Echtler *et al.* 1997), Dabieshan (Faure *et al.* 2003)) and recent mountain belts (Chemenda *et al.* 1995, 2000; west Mediterranean orogen (Caby *et al.* 2001), Hellenides (Xypolias & Koukouvelas 2001), Oman (Gray *et al.* 2004; Searle *et al.* 2004)).

The attention of researchers in the Himalayas has been mainly focused on the structural and metamorphic evolution of the STDS and MCT systems because it is their activity that either allowed the upward and southward extrusion of the wedge of crystalline rocks now exposed in the core of the orogen (Hodges *et al.* 1992) or played a primary role in channel flow models suggested for these crystalline rocks (Grujic *et al.* 1996, 2002). Analogue experiments (Chemenda *et al.* 1995) further support models of tectonic extrusion, whereas numerical experiments (Beaumont *et al.* 2001, 2004; Jamieson *et al.* 2004) better support channel flow models. Although there is an increasing amount of data on the main tectonic boundaries of the wedge- or slab-shaped GHS, very few data are available for the structural and kinematic

From: LAW, R. D., SEARLE, M. P. & GODIN, L. (eds) *Channel Flow, Ductile Extrusion and Exhumation in Continental Collision Zones*. Geological Society, London, Special Publications, **268**, 425–444.
0305-8719/06/$15.00

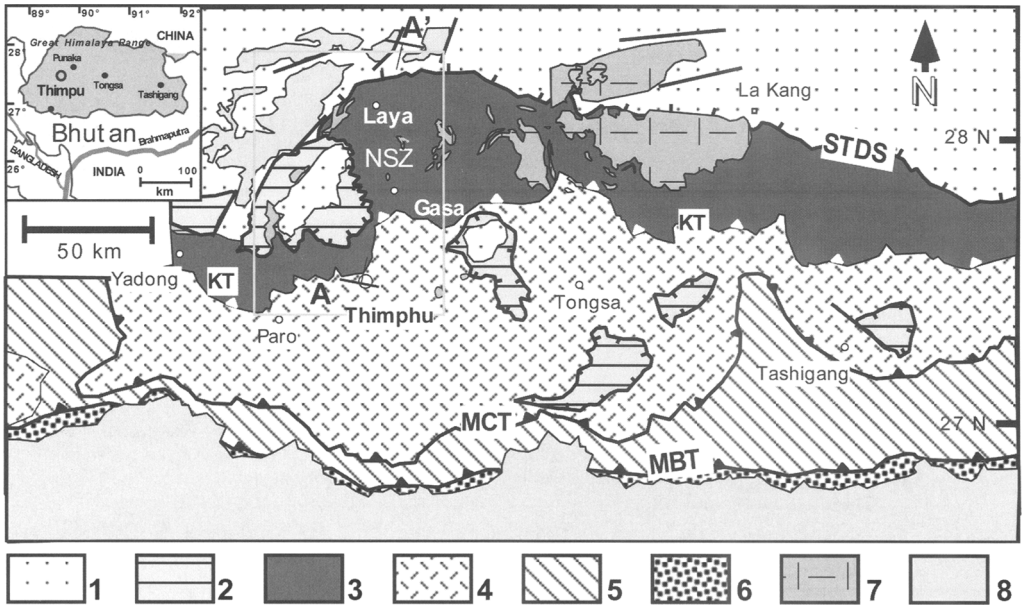

Fig. 1. Geological sketch map of the Bhutan Himalaya (redrawn from Gansser 1983; Grujic *et al.* 2002; Daniel *et al.* 2003) and location of the studied normal shear zones (white rectangle with NSZ; see Fig. 2). 1, Tethyan sediments; 2, Chekha Formation; 3, higher structural levels of the GHS; 4, lower structural levels of the GHS; 5, Lesser Himalayan Sequence; 6, Siwalik; 7, leucogranites; 8, Quaternary sediments. MBT, Main Boundary Thrust; MCT, Main Central Thrust; KT, Kakhtang thrust; STDS, South Tibetan Detachment system. A–A' indicates trace of the geological cross-section in Figure 3.

evolution of its interior (Carosi *et al.* 1999; Vannay & Grasemann 2001).

In this paper, on the basis of recent fieldwork in western Bhutan (Fig. 1), we document the presence of ductile shear zones, exhibiting normal-sense motion, located in the interior of the extruding wedge/slab. The geometry, kinematics, relation with Himalayan granites, age and location of these shear zones seem to be closely related to the exhumation of the metamorphic wedge and could give further constraints on the associated extrusion mechanisms.

A range of tectonic models has been proposed to explain extrusion of the wedge- or slab-shaped metamorphic core of the Himalaya, referred to as the Greater Himalayan Slab (GHS), and these help us to better understand the complex factors affecting the evolution of the mountain belt. However, few field-derived data, especially on the kinematic vorticity number (Passchier 1987) associated with internal penetrative deformation of the GHS (Grasemann *et al.* 1999; Law *et al.* 2004; Jessup *et al.* 2006), are available to better constrain these models. The estimation of kinematic vorticity number associated with shear zone deformation and surrounding matrix in the study area allows us to contribute, with new field-derived data, to the debate over mechanisms of extrusion.

Geological setting

The Himalayan chain resulted from collision between the India and Asia plates starting at 54–50 Ma (Searle *et al.* 1987; Rowley 1988). One of the most striking aspects of this orogen is the lateral continuity of its major tectonic elements (Hodges 2000 and references therein). The main tectonic units building up the chain are, from top to bottom and from north to south: the Tibetan Sedimentary Sequence (TSS), the Greater Himalayan Slab (GHS), the Lesser Himalayan Sequence (LHS) and the Siwalik Group. The TSS comprises a nearly complete sequence of Upper Proterozoic to Eocene sediments deposited on the northern margin of the Indian Plate. The GHS predominantly consists of medium- to high-grade metamorphic rocks made up of pelitic paragneisses with subordinate metacarbonate rocks, calc-schists, amphibolites, granitic orthogneisses and migmatites. Miocene leucogranites are intruded in the upper part of the tectonic unit.

The LHS is mainly formed by a thick sequence of weakly metamorphosed Precambrian sediments and higher metamorphic rocks which overlie the low-grade metasediments. In the upper part of the LHS an inverted metamorphic field gradient from greenschist to lower amphibolite facies has been observed (Le Fort 1975; Arita 1983; Hodges 2000). The Siwalik Group is made up of folded and thrust-faulted molasse sediments of Miocene to Pliocene–Pleistocene age.

The main tectonostratigraphic units of the Himalayan chain have also been recognized in Bhutan (Gansser 1964, 1983) (Fig. 1). First-order tectonic discontinuities border the main tectonic units all along the belt. The Siwalik Group is roofed by the LHS along the Main Boundary Thrust (Le Fort 1975; Gansser 1983). The LHS is overridden by the GHS along the Main Central Thrust (MCT; Auden 1935; Heim & Gansser 1939; Gansser 1964, 1983; Le Fort 1975). Motion on the MCT has been estimated by Daniel *et al.* (2003) to have started as early as 23 Ma in eastern Bhutan.

At the top of the GHS the South Tibetan Detachment System places the GHS in contact with the overlying TSS. In the western Bhutan Himalaya the contact between TSS and GHS occurs within the intervening Chekha Formation (Gansser 1983; Grujic *et al.* 2002) and is marked by top-to-north ductile normal-sense-motion shear zones and an upward abrupt decrease in metamorphic grade. Leucogranite sills and dykes are intruded in the marbles of the Chekha Formation (Gansser 1983), and are often cut by mylonitic fabric related to this top-to-the-north shearing (Grujic *et al.* 2002). It is worth noting here that the STDS is folded into large-scale antiforms and synforms, and klippen of the TSS occur in the cores of synforms in the GHS of the Bhutan Himalaya (Edwards *et al.* 1996, 1999; Grujic *et al.* 2002).

This study focuses on the GHS exposed in western Bhutan. This tectonic unit has been divided into a subunit characterized primarly by gneisses with subordinate migmatites, amphibolites, calc-silicates and biotite schists, and a second subunit composed of pelitic schists, quartzites, calc-silicates, marbles and minor amphibolites (grouped as the Paro metasediments) (Gansser 1983). The GHS is repeated in two stacked tectonic units by the south-directed Kakhtang thrust (Gansser 1983; Swapp & Hollister 1991; Grujic *et al.* 1996) which has been interpreted as an out-of-sequence thrust (Grujic *et al.* 2002) active between 10 and 14 Ma (Daniel *et al.* 2003).

The GHS is characterized by an inverted metamorphic field gradient along the whole length of the belt. This feature has been interpreted in Bhutan as being caused by displacement along the out-of-sequence Kakthang thrust putting migmatites over amphibolite-facies rocks (Swapp & Hollister 1991; Grujic *et al.* 2002). In the hanging wall of the Kakhtang thrust, high-pressure rocks experienced a high-temperature (750–800°C) decompression (from 13 to 5 kb) at 18–16 Ma, following the main deformation and metamorphism of the GHS (Swapp & Hollister 1991; Davidson *et al.* 1997; Daniel *et al.* 2003). In contrast, the footwall rocks of the Kakhtang thrust underwent increasing temperature associated with thrusting of the overlying migmatites and emplacement of leucogranite; this heating event continued to 13 Ma (Davidson *et al.* 1997; Daniel *et al.* 2003). Extrusion of the GHS was responsible for both top-to-the-south and top-to-the-north shearing, with development of fibrolitic sillimanite in shear bands (Grujic *et al.* 1996, 2002). Davidson *et al.* (1997) reported the presence of top-to-the-south and top-to-the-north conjugate shear bands filled by leucosomes in the GHS.

Leucogranite sills and dykes are mainly found in the upper portion of the GHS, especially above the Kakhtang thrust (Dietrich & Gansser 1981; Castelli & Lombardo 1983; Ferrara *et al.* 1991; Davidson *et al.* 1997; Daniel *et al.* 2003).

In the study area, located north of Thimphu, between Gasa and Laya villages (Figs 1 & 2) the predominant rock types are sillimanite-bearing gneisses, minor migmatitic gneisses and small leucogranite bodies and dykes. Swapp & Hollister (1991) indicate, in accordance with the metamorphic facies map distribution proposed by Gansser (1983), a higher amphibolite facies (sillimanite + muscovite + garnet + plagioclase + quartz ± kyanite ± staurolite ± K-feldspar) for the rocks sampled in the study area. The main fabric is a penetrative coarse-grained schistosity (Swapp & Hollister 1991; Davidson *et al.* 1997).

Normal-sense shear zones: geometry and kinematics

Ductile to ductile–brittle shear zones with normal-sense displacement (NSZ) have been recognized in the study area, north of Thimphu between Gasa and Laya villages in the hanging wall of the Kakhtang thrust. They are structurally located in the middle portion of this hanging wall tectonic unit (Figs 1, 2 & 3).

Shear zones are developed from centimetres to tens of metres in size, mainly in sillimanite-bearing gneisses and subordinately in leucogranites. They cross-cut the main (NE-dipping) fabric in the host gneiss at moderate to high angles throughout the studied section (Fig. 4a, c, d). The strike of the shear zones varies between N050° and N085° and

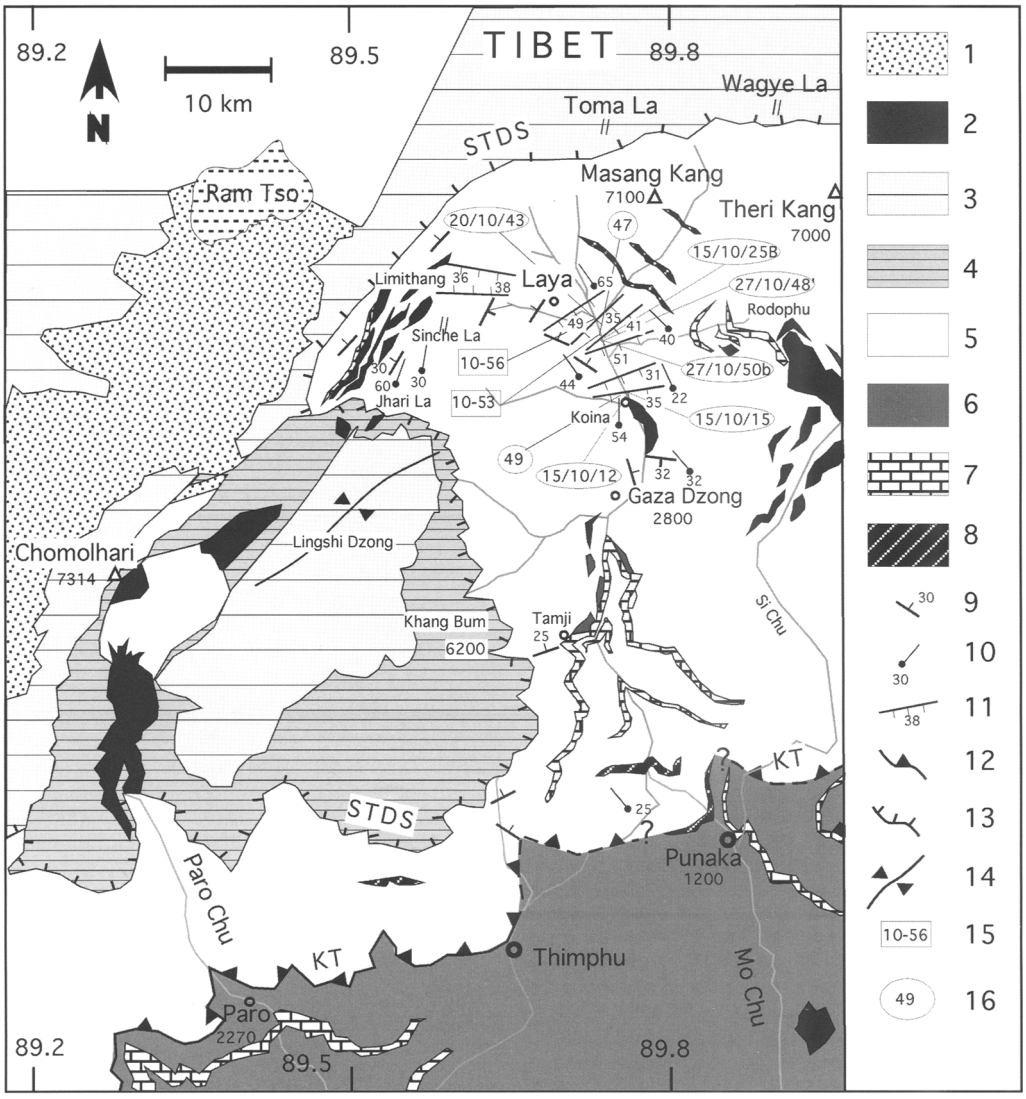

Fig. 2. Geological sketch map of the study area (modified from Gansser 1983; Grujic *et al.* 2002). See Figure 1 for regional setting of the area. 1, Quaternary; 2, leucogranites; 3, Tethyan sediments; 4, Chekha Formation; 5, higher structural levels of the GHS; 6, lower structural levels of the GHS; 7, main bodies of marble; 8, main bodies of amphibolite; 9, main fabric in the sillimanite-bearing gneiss; 10, stretching lineation in sillimanite-bearing gneiss; 11, top-to-the-SE normal-sense shear zones; 12, out-of-sequence Kakhtang thrust; 13, South Tibetan Detachment System; 14, Lingshi synform; 15, location of sample for geochronological studies; 16, location of vorticity analysis samples.

they dip towards the SE (35–50°) (Fig. 5). Stretching lineation on shear planes is well developed, plunges moderately towards the SE and is marked by quartz, sillimanite, tourmaline and biotite (Fig. 4b).

Mylonites and a thin layer of ultramylonite are developed in the sillimanite-bearing gneiss and leucogranites deformed within the shear zones, and range from centimetres to tens of metres in thickness (Fig. 4). Kinematic indicators are well developed both at the meso- and microscale (Figs 4 & 6). At the mesoscale, kinematic indicators are mainly represented by shear bands, asymmetric foliation boudinage and foliation fish. At the microscale (Fig. 6) mica fish, delta and sigma

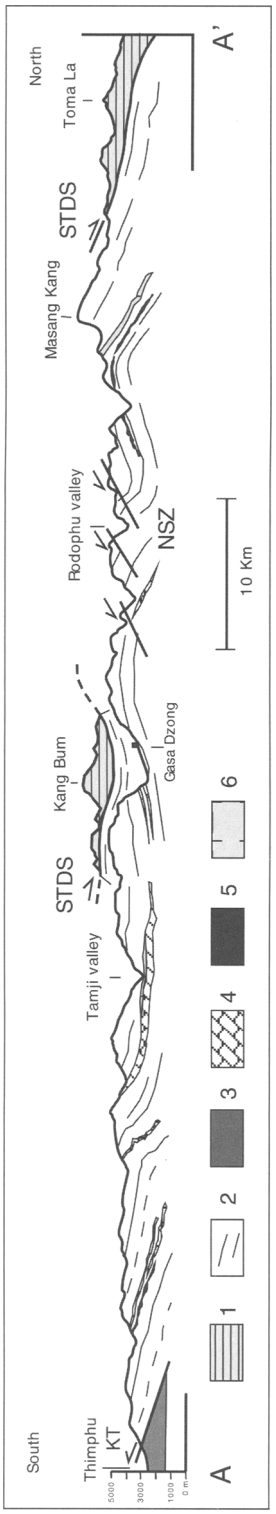

Fig. 3. Geological cross-section through the Greater Himalyan Sequence in western Bhutan. See trace in Figure 1 (modified after Gansser 1983). 1, Tethyan sediments and Chekha Formation; 2, higher structural levels of the GHS; 3, lower structural levels of the GHS; 4, marbles; 5, amphibolites; 6, leucogranites. KT, Kakhtang thrust; NSZ, normal-sense shear zones; STDS, South Tibetan Detachment System.

porphyroclasts, C-S fabric, synthetic and antithetic fractures (especially in feldspar and tourmaline porphyroclasts) are well developed. Myrmekite occurs on surfaces of feldspar grains that are orientated orthogonal to the maximum shortening direction. All kinematic indicators point to a top-down-to-SE and SSE sense of shear, i.e. a normal-sense motion.

Quartz shows evidence of crystalline plasticity with undulatory extinction, subgrains and new grains, and grain boundary migration. Well-preserved quartz ribbons wrap around feldspar porphyroclasts. Elongate dynamically recrystallized quartz grains aligned oblique to foliation in ribbon quartz are frequently observed. Garnet, kyanite and sillimanite crystals are deformed by shear bands within the mylonites. Larger sillimanite crystals are fractured and often boudinaged along the main fabric with tensile fractures filled by quartz and biotite (Fig. 4b). The growth of fibrolitic and prismatic sillimanite crystals along shear bands in the mylonites indicates that top-to-the-SE deformation in normal shear zones occurred at close to peak metamorphic temperatures. However, in some mylonites low temperature deformation mechanisms have been detected, suggesting a temporal progression of shear deformation towards higher structural levels.

Two bodies of deformed leucogranite (two-mica leucogranite and biotite-tourmaline leucogranite: classification according to Visonà & Lombardo 2002) cross-cut, but are also deformed within, the normal-sense-motion shear zones. In one case, centimetre- up to decimetre-sized NSZ, characterized by a concentration of tourmaline crystals, cross-cut undeformed to slightly deformed biotite granite bodies. A few kilometres north of Koina (Fig. 2), in the direction of Laya, a two-mica leucogranite is emplaced and deformed within centimetre- to decimetre-sized NSZ (Fig. 7). The overprinting relations between granites and shear zones developed within sillimanite-bearing gneisses potentially help to constrain the age of motion on the shear zones.

Brittle normal faults, also showing a top-down-to-the-SE sense of movement, are superimposed on the ductile normal shear zones. They strike NE–SW and dip moderately to the SE (50–60°). Slickenside striae on these faults plunge at 30–40° to the SE. Cataclasites and ultracataclasites with minor development of pseudotachylite can be recognized. These faults may be of the same age as an earlier system of normal faults reported by Wiesamayr *et al.* (2002) in the nearby leucogranites and migmatites of the Lunana region (central Bhutan). However, we did not observe the fault rotation reported by Wiesamayr *et al.* (2002) for the earlier fault system in our study transect.

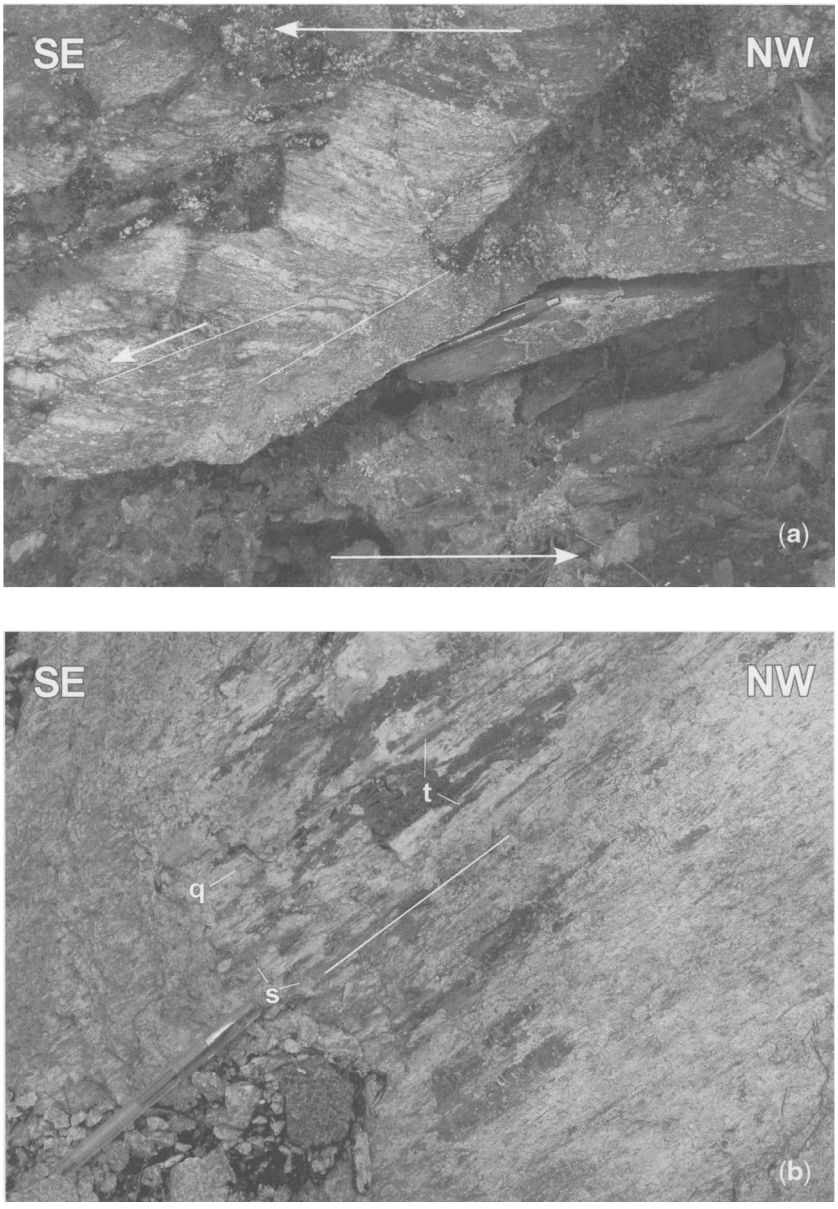

Fig. 4. Outcrop examples of normal-sense shear zones cutting sillimanite-bearing gneisses in the interior of the GHS. Localities are all from Gasa and Laya villages (see Fig. 2). Sense of shear is top-down-to-the-SE. (**a**) Shear planes and mylonites. (**b**) Stretching lineation marked by quartz (q), tourmaline (t) and sillimanite (s) on a shear plane near Koina village. (**c**) Mylonites (m) cross-cutting main fabric of the sillimanite-bearing gneisses dipping to the north (upper part of the picture). (**d**) Close-up view of mylonitic shear bands (m) cross-cutting sillimanite-bearing gneisses (gn) dipping to the north (centre part of the picture).

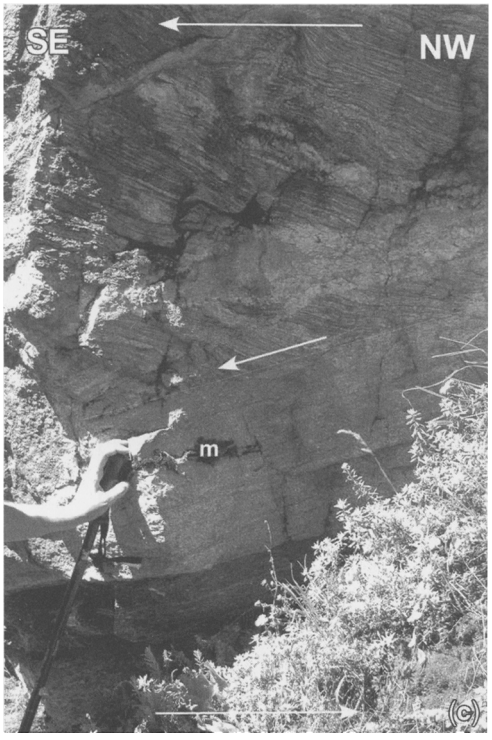

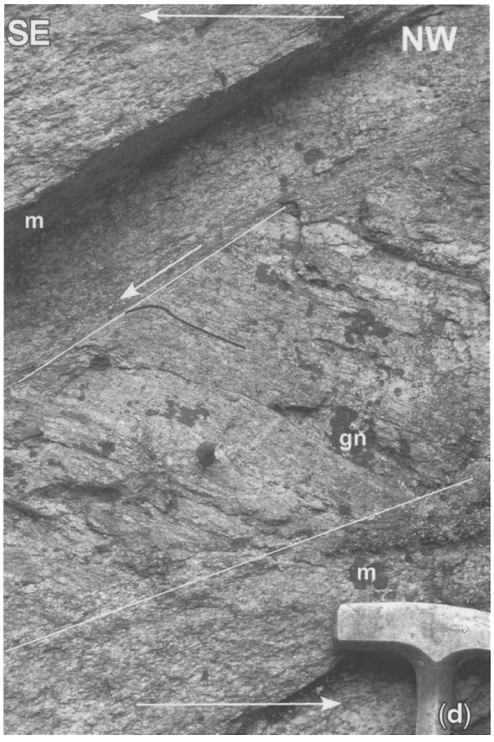

Fig. 4. (*Continued*).

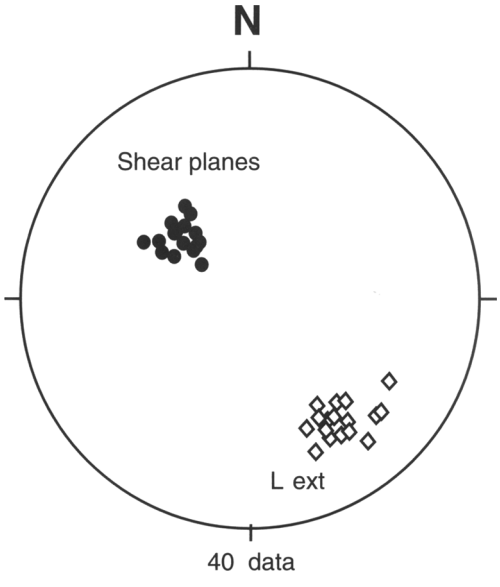

Fig. 5. Stereographic projections of stretching lineations and poles to foliation from the studied top-to-the-SE NSZ. Lower hemisphere.

Vorticity analysis

Vorticity analysis was carried out to investigate the degree of non-coaxiality of flow during deformation and shear zone development. A steady-state general shear deformation could develop as a result of pure and simple shear components of deformation acting simultaneously (Simpson & De Paor 1983; Hudleston 1999).

The degree of non-coaxiality of the flow can be expressed by the mean kinematic vorticity number (*Wm*; Passchier 1987) that describes the bulk rotation of material lines coincident with the principal strain axes (*Wm* is the ratio between the mean angular velocity of lines and the stretching rates). In a pure shear deformation $Wm = 0$, while in simple shear deformation $Wm = 1$. The two components, pure and simple shear, make an equal contribution to the instantaneous flow at $Wm = 0.71$ (Law *et al.* 2004).

In this study the mean kinematic vorticity number *Wm* has been estimated following the method proposed by Passchier (1987) and Wallis *et al.* (1993). This method is based on measuring the orientation θ and aspect ratio (R: $Rmax/Rmin$) of rigid porphyroclasts rotating in a ductile matrix until they reach stable orientations corresponding

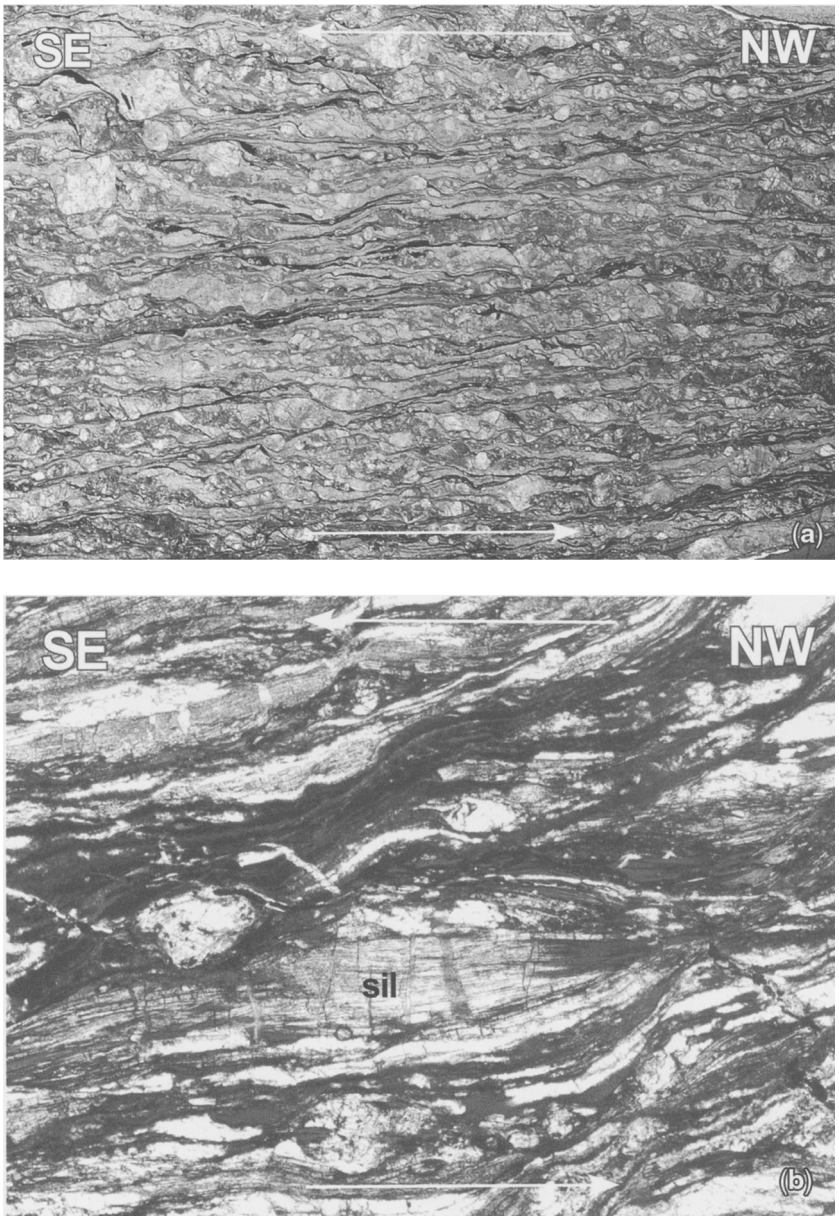

Fig. 6. Microphotographs from mylonites in NSZ. (**a**) C' shear planes and sigma-type porphyroclasts. Field of view is 2.4 cm. (**b**) Stretched sillimanite crystal along S surface with tension fractures filled with biotite. Field of view is 8 mm.

to a critical aspect ratio (*Rc*). Porphyroclasts with an aspect ratio lower than the critical value (*Rc*) rotate continuously in the matrix, while those with an aspect ratio higher than *Rc* reach a stable orientation. The *Rc* values are linked to vorticity (*Wm*) by the following relation (Wallis *et al.* 1993):

$$Wm = (Rc^2 - 1)/(Rc^2 + 1)$$

Analyses were carried out on eight samples (Fig. 8), six from the shear zones and two from the surrounding gneiss. Measurements were conducted on thin sections cut parallel to the stretching lineation and perpendicular to the foliation. It is assumed that these sections approximate the XZ plane of finite strain ellipsoid and are orientated perpendicular to the vorticity vector in a monoclinic shear zone.

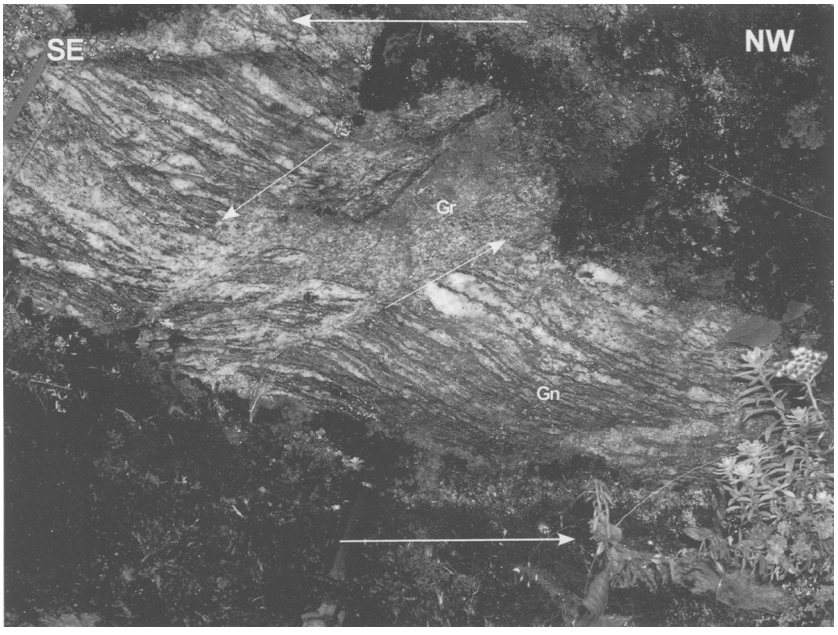

Fig. 7. Two-mica leucogranite (Gr) (sample 10-53) mylonitically deformed within centimetre-size top-to-the-SE NSZ in high-grade gneisses (Gn) (north of Koina village; Fig. 2).

The most suitable minerals in our samples for this rigid grain method of vorticity analysis are plagioclase and K-feldspar porphyroclasts. We selected isolated and non-fractured porphyroclasts coarser than the surrounding matrix. Other minerals, such as tourmaline (abundant in the leucogranitic sample) have been avoided as they are strongly fractured with separation of fragments. For each sample the axial ratios of 66 to 161 porphyroclasts were measured and plotted against the orientation of their long axes (relative to foliation) in order to estimate the *Rc* value for each sample (Fig. 8). It is sometimes difficult to find an exact value of *Rc* from the scattered points on the $R-\theta$ diagrams and a range of *Rc* values has been estimated for each graph. Following Law *et al.* (2004) we indicate a minimum and a maximun *Rc* value for each sample (Fig. 8). The average variation of *Rc* is 0.4 causing a mean variation of the calculated *Wm* of nearly ± 0.1.

Estimated mean kinematic vorticity numbers (*Wm*) vary between 0.63 and 0.76 with a mean value of 0.68 for the shear zones (Fig. 8). This indicates an important pure shear component during shear zone development. In the surrounding gneiss *Wm* varies between 0.67 and 0.76, with a mean value of 0.68 (Fig. 8).

The flow apophysis A1 (apophysis parallel to the foliation) is in a different orientation in the NSZ relative to its orientation in the surrounding country rocks. While in the NSZ A1 is inferred to be parallel to the boundaries of the shear zones themselves, so that it dips towards the SE, in the country rocks A1 is parallel to the main north-dipping tectonic discontinuities bounding the extruding GHS (MCT and STDS) (Fig. 1). The mean vorticity numbers (*Wm*) obtained from these discrete shear zones, however, are very similar to the *Wm* values obtained from the surrounding country rocks. We therefore argue that the calculated *Wm* values describe the regional flow pattern associated with southward extrusion of the GHS. Even if deformation is partitioned between the country rock and the NSZ, the estimated vorticity of the flow is the same. If there are true differences in vorticity values, as we might expect to find in high-strain shear zones with respect to their surrounding country rocks, these differences are not detectable within the uncertainties in estimated *Wm* values.

U–Pb geochronology

Sample and zircon description

Granite samples were selected from two outcrops located nearly half-way between the villages of Gasa and Laya (Figs 1 & 2) where extensional shear zones and granites are in close contact. The

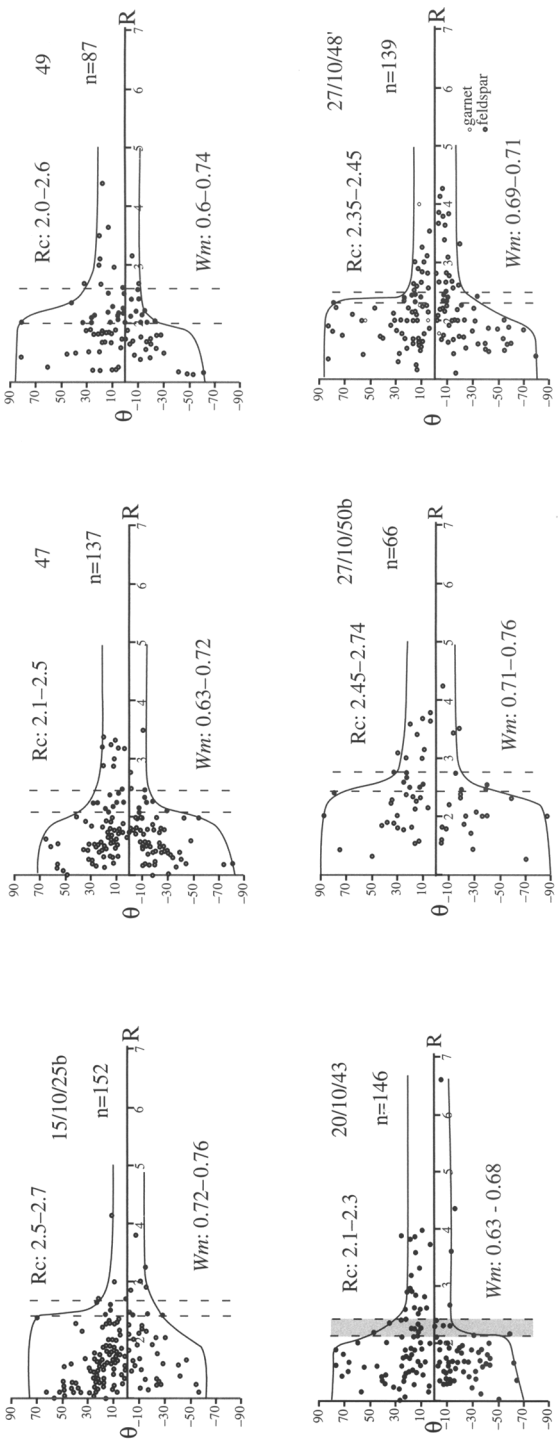

Fig. 8. Graphs for porphyroclast-based vorticity analyses (after Passchier 1987; Wallis *et al.* 1993; Wallis 1992, 1995). Samples 47 and 49 are from the sillimanite-bearing gneiss outside NSZ; sample 15-10-25b is from leucogranite; remaining samples are from mylonites in normal shear zones. R, Aspect ratio of porphyroclast; θ, angle between long axis of porphyroclast and foliation (a positive angle indicates porphyroclast long axis is inclined in top-to-the-south shear sense; a negative angle indicates long axis is inclined against shear sense); *Rc*, critical aspect ratio below which clasts are inferred to continuously rotate and above which they attain a stable orientation; *Rc*, the critical aspect ratio; for each sample, range of uncertainty of *Rc* is given (dashed vertical lines); *n*, number of measured grains in each section; *Wm*: mean vorticity kinematic number.

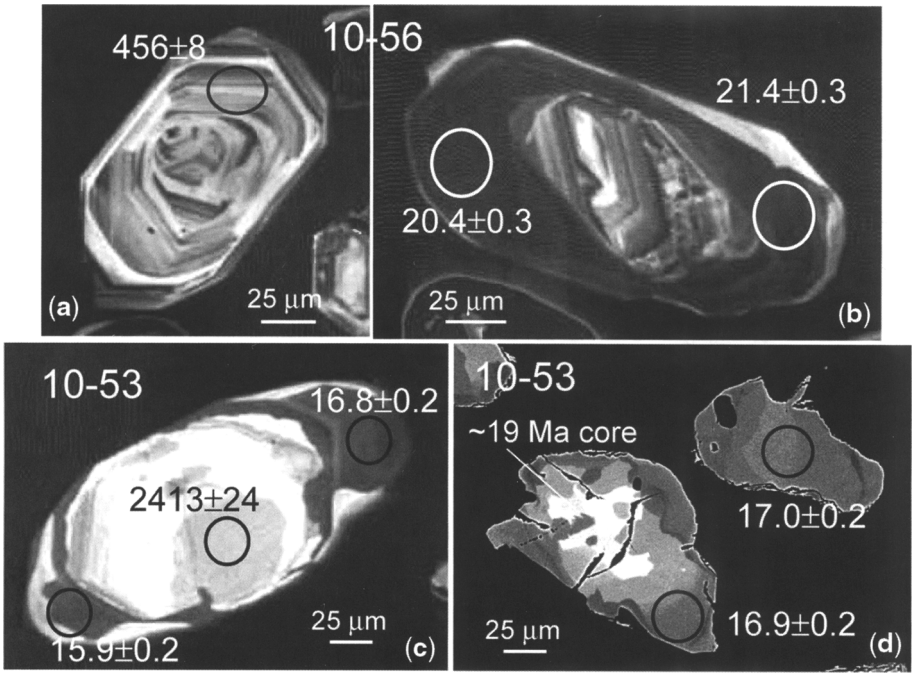

Fig. 9. Cathodoluminescence images of zircon crystals analysed by SHRIMP from sample 10-56 and 10-53 (**a–c**), and BSE images of monazite from sample 10-53 (**d**). Circles indicate location of analyses for which $^{208}Pb/^{238}U$ ages in Ma are reported. Errors are at 1 sigma level.

two samples came from the same structural level within the GHS, but were collected 5 km apart. In the first outcrop (sample 10-56, Fig. 2) a weakly deformed biotite granite, intruded in sillimanite-bearing gneisses, is cross-cut by centimetre-sized NSZ with the same orientation as the other NSZ in the area. In the lower part of the outcrop a thick NSZ post-dates this biotite granite and deforms a tourmaline leucogranite producing a mylonitic C-S fabric orientated parallel to the NSZ boundaries, and indicating a top-to-the-SE sense of shear.

The second outcrop is characterized by emplacement of a two-mica leucogranite (sample 10-53, Fig. 2) within a NSZ which cross-cuts the main fabric in the surrounding sillimanite-bearing gneiss (Fig. 7). Three apophyses emanate from the main granitic body and are emplaced along a 3-cm NSZ; a mylonitic fabric is developed within these granitic apophyses. This relationship suggests that granite generation, its emplacement and deformation, occurred approximately synchronously.

Zircons were extracted from both samples. Sample 10-56 contains zircon crystals that are commonly euhedral, pink to colourless and transparent. Two different zircon types can be recognized on the basis of the zoning pattern observed in cathodoluminescence (CL). The majority of the crystals have a well-defined oscillatory zoning with bands parallel to the crystal faces (Fig. 9). Some of these crystals may preserve a core with variable zoning pattern, and occasionally the core can be volumetrically more important than the oscillatory domain. Approximately 10% of the grains are characterized by a dark, weakly zoned domain that can either overgrow the oscillatory zircon or represent the entire crystal section (this could be related to a 'cut effect'). The dark domain is often surrounded by a very thin rim (1–5 μm across) with brighter CL emission and in which no zoning can be recognized (Fig. 9). Given that the sample is composed of a granite cross-cut by a NSZ, it is likely that the oscillatory-zoned zircon is associated with crystallization of the granite, whereas the dark, less abundant, zircon crystals may be related to the cross-cutting mylonitic tourmaline granite.

Sample 10-53 is a two-mica mylonitic leucogranite deformed within a shear zone (Fig. 7). This leucogranite contains zircon crystals that are mainly euhedral, clear, transparent and colourless. In cathodoluminescence they have a composite structure characterized by variable CL emission and zoning patterns. In the majority of the crystals

the zoning is oscillatory. A few grains have a dark, poorly zoned overgrowth on the more complex core (Fig. 9). Monazite crystals recovered from the same sample are small (≤100 μm) and anhedral. In backscattered electron (BSE) imaging the monazite crystals display rare, bright cores surrounded by a more homogeneous domain with medium BSE emission (Fig. 9). These domains can have weak zoning with a banded or patchy pattern; cores are present in only a few of these grains.

Analytical methods

Zircon was prepared as mineral separates mounted in epoxy and polished down to expose the grain centres. Cathodoluminescence (CL) and backscattered electron (BSE) investigation was carried out at the Electron Microscope Unit, Australian National University. CL was performed with a Hitachi S2250-N scanning electron microscope working at 15 kV, *c.* 60 μA and *c.* 20 mm working distance. BSE imaging was carried out with a Cambridge S360 scanning electron microscope using a voltage of 20 kV, current of *c.* 3 nA and a working distance of *c.* 20 mm.

U–Th–Pb analyses were performed using a sensitive, high-resolution ion microprobe (SHRIMP RG). Instrumental conditions and data acquisition were generally as described by Compston *et al.* (1984). The data were collected in sets of seven scans throughout the masses. The measured $^{206}Pb/^{238}U$ ratio was corrected using reference zircon from the Middledale Gabbroic Diorite (417 Ma; Black *et al.* 2003), whereas a zircon of known composition (SL 13) has been used to determine the U content of the target. Analyses for both zircon and monazite were corrected for common Pb on the basis of the measured $^{207}Pb/^{206}Pb$, as described by Compston *et al.* (1984). The composition of the common Pb has been assumed to be that of Broken Hill galena ($^{204}Pb/^{206}Pb = 0.06250$, $^{207}Pb/^{206}Pb = 0.96180$, $^{208}Pb/^{206}Pb = 2.22850$), which is known to be common Pb instrumental background. Age calculations were done using the software Isoplot/Ex L (Ludwig 2000). Isotopic ratios and single ages are reported with 1σ errors, whereas mean ages are at 95% confidence level.

Results and interpretation

SHRIMP analysis of zircon from sample 10-56 was focused on the oscillatory zoned domains and the dark overgrowths. The oscillatory domains have variable U and Th contents and variable Th/U composition (Table 1). The $^{206}Pb/^{238}U$ ages scatter between 112 and 514 Ma, and a number of analyses are discordant. Even when only the $^{207}Pb/^{206}Pb$ ages are considered, which should give a minimum age for the zircon formation, the scatter is still large (395–497 Ma). This data dispersion, together with the variable Th and U composition, indicates that the different oscillatory zircon crystals dated do not come from the same source, but are a composite population that is at least in part inherited. What can be concluded is that the granite, or its source, has a minimum age of 397 ± 8 Ma, which is the age of the youngest concordant oscillatory zircon dated. A younger age cannot be excluded because the analyses on the oscillatory domains were limited in number and a younger component might have been missed.

The dark zircon domains are extremely rich in U (2280–15 700 ppm) and poor in Th (16–441 ppm), resulting in low Th/U ratio (<0.03). Such low ratios are generally observed either in low-temperature metamorphic zircon formed in subsolidus conditions (≤600°C; e.g. Rubatto & Gebauer 2000; Hoskin & Schaltegger 2003) or in anatectic melts formed by a low degree of partial melting (e.g. Williams *et al.* 1996). The ages of the dark zircon domains scatter over a significant range from *c.* 31 to 15 Ma. Several factors have to be considered to explain this age scatter. Two analyses yielding the oldest ages were recognized as being mixed between a dark domain and an inherited core and are thus not further considered. Two analyses at around 23 Ma yielded extreme U concentrations (12 100 and 15 700 ppm). High U has been recognized as responsible for matrix effects in SHRIMP analyses (the standard used contains only a few hundred ppm of U) leading to older ages with increasing U content (Butera *et al.* 2001). Even though in this sample a correlation between U content and age was not observed, the two analyses with high U content were excluded because of likely matrix effects. Of the remaining 14 analyses, nine define a major group at around 20.5 Ma, one is older and close in age to the extremely high U domains, whereas the other four analyses are significantly younger. The four younger analyses, which do not form a cluster but scatter between 18.0 ± 0.2 and 14.9 ± 0.2 Ma, are likely to have been affected by partial lead loss. The granite and the tourmaline mylonite, to which the dark zircon crystals are likely to belong, are intensely deformed and the zircon probably suffered some Pb loss due to fracturing and fluid leaching. The nine analyses forming the main cluster are poor in common Pb and plot on or very close to concordia in a Tera-Wasserburg diagram (Fig. 10a). Assuming the common Pb to be that of Broken Hill (see Methods), the analyses define an average age of 20.5 ± 0.5 Ma with a relatively large MSWD of 6, which indicates a certain dispersion of the data above analytical uncertainty. However,

Table 1. *U–Pb analyses by SHRIMP on separated zircons and monazites from samples 10-56 and 10-53*

Spot name	Pb com (%)	U (ppm)	Th (ppm)	Th/U	Total $^{238}U/^{206}Pb$	$\pm 1\sigma$	Total $^{207}Pb/^{206}Pb$	$\pm 1\sigma$	Age $^{206}Pb/^{238}U$	$\pm 1\sigma$	Discordance (%)
Zircon											
1056-2.2	0.00	1342	556	0.414	12.02	0.19	0.0578	0.00026	515	8	−7
1056-11	0.01	1496	128	0.086	12.47	0.21	0.0569	0.00026	498	8	−12
1056-25.1	0.02	2974	32	0.011	13.26	0.18	0.0579	0.00018	468	6	6
1056-10	0.18	884	354	0.400	13.61	0.25	0.0576	0.00066	456	8	−13
1056-12	1.29	1271	546	0.430	15.70	0.32	0.0570	0.00045	397	8	−1
1056-14	0.00	2576	28	0.011	20.53	0.33	0.0577	0.00028	305	5	50
1056-24.1	0.04	4609	19	0.004	56.91	0.66	0.0563	0.00144	111	1	274
1056-23.2	0.18	3324	16	0.005	207.6	3.9	0.0520	0.00075	30.8	0.6	
1056-13.2	39.52	4690	42	0.009	140.9	1.8	0.4220	0.02305	26.9	2.4	
1056-30	0.10	15707	441	0.028	271.7	3.5	0.0474	0.00038	23.7	0.3	
1056-22.1	0.06	12130	81	0.007	278.0	3.3	0.0475	0.00052	23.1	0.3	
1056-18.2	0.06	4269	16	0.004	285.5	3.6	0.0483	0.00073	22.5	0.3	
1056-22*	0.03	8992	61	0.007	298.6	3.7	0.0479	0.00053	21.5	0.3	
1056-15*	0.11	7422	41	0.006	299.7	4.8	0.0480	0.00052	21.4	0.3	
1056-13*	0.08	5251	25	0.005	301.1	5.0	0.0474	0.00066	21.4	0.4	
1056-23.1*	0.12	6621	31	0.005	311.5	3.7	0.0496	0.00054	20.6	0.2	
1056-15.2*	0.59	2282	27	0.012	309.6	4.2	0.0651	0.00322	20.4	0.3	
1056-20.1*	0.09	6567	68	0.010	319.3	3.8	0.0474	0.00053	20.1	0.2	
1056-16*	0.11	5914	37	0.006	321.7	5.4	0.0481	0.00060	20.0	0.3	
1056-18.1*	0.13	5311	17	0.003	323.8	3.9	0.0482	0.00070	19.8	0.2	
1056-21.1*	0.08	7684	120	0.016	329.6	5.5	0.0474	0.00052	19.5	0.3	
1056-19.1	1.13	2390	56	0.024	356.7	4.7	0.0487	0.00107	18.0	0.2	
1056-20.1	0.07	8315	23	0.003	359.0	6.0	0.0465	0.00081	17.9	0.3	
1056-31.1	0.43	5850	31	0.005	384.1	4.8	0.0490	0.00080	16.7	0.2	
1056-26	0.09	6145	33	0.005	431.9	5.2	0.0460	0.00062	14.9	0.2	
1053-3.1	0.20	3478	74	0.022	471.9	4.0	0.0482	0.0010	13.6	0.1	
1053-4.1	8.23	4167	49	0.012	389.1	3.1	0.1217	0.0052	15.2	0.2	
1053-1.2	0.54	1218	34	0.029	403.6	4.1	0.0513	0.0019	15.9	0.2	
1053-1.1*	0.16	1283	30	0.024	380.3	3.7	0.0479	0.0014	16.9	0.2	
1053-2.1*	0.31	2051	13	0.006	378.2	3.4	0.0492	0.0012	17.0	0.2	
1053-2.2*	0.10	2224	14	0.007	378.8	3.3	0.0473	0.0011	17.0	0.2	
1053-3.2	0.76	2854	53	0.019	72.49	0.70	0.0547	0.0005	87.7	0.9	321
1053-4.2	0.02	1151	91	0.082	12.62	0.09	0.0571	0.0003	491	4	−1
1053-1.3**	1.68	81	83	1.064	2.20	0.03	0.1666	0.0009	2413	24	4

(*Continued*)

Table 1. *Continued*

Spot name	Pb com (%)	U (ppm)	Th (ppm)	Th/U	Total $^{238}U/^{206}Pb$	$\pm 1\sigma$	Total $^{207}Pb/^{206}Pb$	$\pm 1\sigma$	Age $^{206}Pb/^{238}U$	$\pm 1\sigma$	Discordance (%)
Monazite											
1053-1.1	1.5	22063	n.a	–	567.1	10.5	0.05995	0.00071	11.36	0.21	
1053-5	4.5	6071	n.a	–	477.3	9.5	0.08720	0.00168	13.49	0.27	
1053-7	1.1	14531	n.a	–	468.4	8.9	0.05679	0.00055	13.75	0.26	
1053-8	1.2	11162	n.a	–	422.1	9.5	0.05778	0.00067	15.25	0.34	
1053-6*	2.1	7797	n.a	–	385.5	8.2	0.06531	0.00114	16.70	0.36	
1053-11*	1.6	9664	n.a	–	385.1	8.2	0.06099	0.00095	16.72	0.35	
1053-9*	1.6	8181	n.a	–	381.2	7.4	0.06150	0.00090	16.89	0.33	
1053-10*	1.7	8233	n.a	–	379.3	7.5	0.06219	0.00098	16.97	0.33	
1053-3*	1.8	9354	n.a	–	375.6	7.8	0.06247	0.00097	17.14	0.35	
1053-2*	2.9	8652	n.a	–	368.2	6.9	0.07271	0.00096	17.49	0.33	
1053-12*	2.0	6962	n.a	–	361.7	7.0	0.06499	0.00099	17.80	0.34	
1053-13 core	1.8	10823	n.a	–	337.5	6.5	0.06326	0.00072	19.07	0.37	
1053-4 core	2.0	8515	n.a	–	335.6	6.7	0.06434	0.00100	19.18	0.38	

*Analysis used to calculate the average age.
**Analysis for which ^{204}Pb corrected age is given.
n.a., Not analysed.

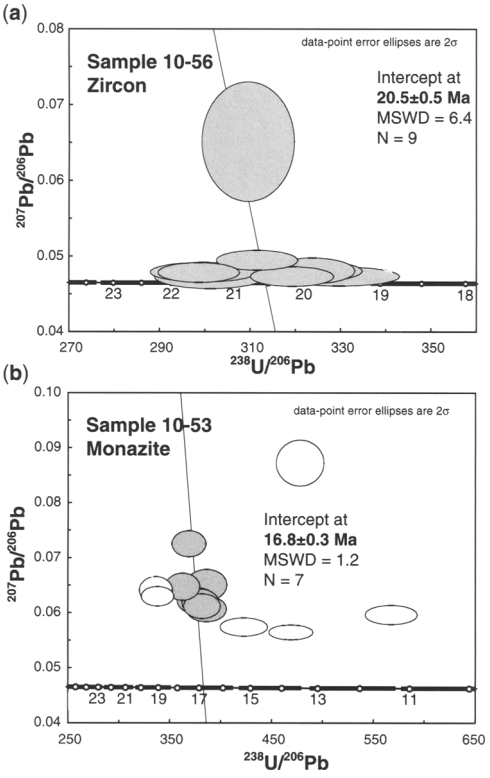

Fig. 10. Tera-Wasserburg diagram for uncorrected data from dark zircon overgrowths in sample 10-56 (**a**), and monazite in sample 10-53 (**b**). Intercept age is reported at 95% confidence level. White ellipses in (b) are excluded from the age calculation. See text for comments on the large MSWD value in (a).

in the absence of criteria for excluding any of the nine data points, and given that these ages are between 19.5 ± 0.3 and 21.5 ± 0.3 Ma, we propose 20.5 ± 0.5 Ma as the best estimate for formation of the dark zircon domains.

A limited number of SHRIMP analyses were performed for sample 10-53, due to the few zircon crystals recovered from the small sample available (Table 1). Two analyses on zoned cores, which have different zoning patterns and U and Th composition, are concordant at 491 ± 4 and 2413 ± 24 Ma. These again suggest a complex inherited zircon population in the granite. Similarly to sample 10-56, the dark overgrowths are rich in U (1220–4170 ppm) and poor in Th with a Th/U ratio below 0.03. They yielded ages from 17.0 to 13.6 Ma, which do not cluster. Three of the six analyses are virtually identical and average at 17.0 ± 0.2 Ma. This is the best age estimate for formation of the zircon overgrowths.

Monazite from sample 10–53 yielded ages scattering between 11.7 and 19.4 Ma. Two monazite cores yielded the oldest ages at 19.1 and 19.2 Ma. The main population (seven out of 13 analyses) forms a tight cluster that defines an age of 16.8 ± 0.3 Ma (intercept on a Tera-Wasserburg diagram assuming Broken Hill common lead, Fig. 10). Four analyses scatter down to 11.5 Ma and are suspected of Pb loss. While the main monazite population is likely formed during granite crystallization, the significance of the 19 Ma cores is unclear. The most likely interpretation is that monazite cores were inherited from the granite source, as often also observed in zircon.

Discussion

Fieldwork in the GHS of western Bhutan has identified a system of widespread metre-to decametre-sized ENE–WSW striking normal shear zones, showing a top-down-to-the-SSE sense of shear, in a structurally high-level section of the unit. These shear zones cross-cut the main deformation fabric and post-date Barrovian minerals in the sillimanite-bearing gneisses. They are found in the interior of the GHS and, up to now, no traces of similar top-to-the-south normal-sense shear zones cutting foliation with an extensional geometry have been reported approaching either the STDS or the MCT zones in western Bhutan. The NSZ geometry and kinematics point to a north–south lengthening of the interior of the GHS.

Wiesamayr *et al.* (2002) have described a system of top-to-the-south normal faults in the eastern Lunana area (central-western Bhutan). These faults cannot be correlated with the NSZ in the study area because they are associated with brittle deformation and, moreover, apparently develop later in the tectonic history as they have been related to activity on the out-of-sequence Kakhtang thrust (Wiesamayr *et al.* 2002). However, our NE–SW striking normal brittle faults could accommodate the NW–SE extension indicated by an earlier system of normal faults reported by Wiesamayr *et al.* (2002).

SHRIMP U–Pb ages on the rims of zircons obtained from sheared leucogranites indicate Himalayan recrystallization. The dark overgrowths on inherited cores have characteristics typical of anatectic melts and leucosomes, i.e. euhedral shape, dark CL emission, poor zoning, very low Th/U ratio (e.g. Williams *et al.* 1996; Hoskin & Schaltegger 2003). Therefore, we interpret the age of the dark overgrowths as dating leucogranite crystallization. The age obtained from the main monazite population in sample 10-53 is interpreted as dating granite crystallization in agreement with the zircon data.

Sample 10-56 is a weakly deformed biotite granite cross-cut by a tourmaline granite that has been intensely mylonitically deformed after crystallization. The dark zircon crystals belong to the tourmaline-rich mylonite, rather than the granite, because of their extreme U composition and low abundance. The age of 20.5 $\pm$ 0.5 Ma constrains the upper time limit for deformation.

Sample 10-53 is a two-mica leucogranite mylonitically deformed along centimetre- to decimetre-sized shear zones (Fig. 7). The ages obtained from zircon overgrowths and monazite indicate that shear zone activity, melt generation and emplacement occurred over a short time period at around 17 Ma. It is relevant that leucogranite 10-53 has no trace of the 20.5 Ma component found in sample 10-56. The two melts were clearly generated in two separate episodes and shearing occurred between 20.5 and 17 Ma or, more likely, close to 17 Ma.

The two different granite ages at 20.5 and 17.0 Ma suggest long-lasting activity for magma generation during ductile extrusion of the high-grade gneisses of the GHS in the Bhutan Himalaya, as suggested by Daniel *et al.* (2003). The age of normal-sense motion on the shear zones is in agreement with both data on exhumation of the GHS in eastern Bhutan and with the prolonged activity of the STDS and MCT, where multiple generations of leucogranites were intruded and defomed from 23 to 13–11 Ma (Davidson *et al.* 1997; Edwards & Harrison 1997; Daniel *et al.* 2003).

Vorticity analyses performed on suitable mylonite samples along a 10 km transect point to a general shear deformation. It is worth noting that this general shear indicates an important pure-shear component during shear-zone activity since the mean vorticity values (*Wm*) are bracketed between 0.63 and 0.76, with a mean value of 0.68, indicating a 53% pure-shear component (see graph in fig. 9 of Law *et al.* 2004).

The component of pure shear associated with internal flow and penetrative deformation of the GHS is independently indicated by the presence of a system of nearly east–west striking and gently dipping conjugate normal shear zones occurring in the sillimanite-bearing gneisses a few hundred metres above Limithang (NW of Laya; Fig. 2). These conjugate shear zones cross-cut the main foliation in the gneisses, and decimetre- to metre-thick tabular leucogranite bodies are penetratively deformed within the shear zones (see also Daniel *et al.* (2003) for eastern Bhutan).

A component of pure shear in the GHS fits well with a wedge-shaped geometry for the GHS delimited by faults or shear zones converging at depth (Burchfiel *et al.* 1992; Hodges *et al.* 1992; Nelson *et al.* 1996; Grasemann *et al.* 1999). As suggested by Ramsay & Huber (1987) and Grasemann *et al.* (1999), shear zones characterized by non-parallel boundaries, or with deforming boundaries, must deform by general shear (i.e. deviate from simple shear) and/or undergo a volume change. A pure-shear component is also required in the channel flow model proposed by Grujic *et al.* (1996, 2002) and Daniel *et al.* (2003), even if the boundaries of the channel are parallel. Moreover, Grujic *et al.* (2002) argue that vorticity is not constant in a channel flow because it is implicit in the velocity field of the Poiseuille flow component that vorticities will be highest against the channel boundaries and lowest in the middle of the channel.

This information, together with the observation that top-down-to-the-SE normal shear zones have been recognized only in the middle part of the GHS exposed in Bhutan and in the Everest section (Carosi *et al.* 1999), is important for better characterizing the kinematics of the whole GHS and its exhumation mode. If we consider the few available data along the belt we can see that approaching the STDS, at the top of the GHS, vorticity *Wm* changes, pointing to a major component of simple shear (Law *et al.* 2004; Jessup *et al.* 2006). The kinematics along the MCT seems to be quite complex. In fact, Grasemann *et al.* (1999) identified an initial prevailing simple shear, evolving into an increasingly pure-shear-dominated flow with lowering temperature during extrusion (see Jessup *et al.* 2006). Vorticity data obtained from the MCT zone in western Nepal indicate *Wm* values higher than 0.71 (R. Carosi, unpublished data). Even if the vorticity values are still scattered along the belt and a complete analysis along a single transect from MCT up to the STDS is still lacking, the available data indicate that the GHS deformed by general non-coaxial ductile flow. The spatial changes in vorticity, *Wm*, indicate an increase in pure shear during extrusion moving from the boundaries to the interior of the GHS (Fig. 11).

Due to strain compatibility requirements (Ramsay 1980), since no structural discontinuities orientated parallel to the main tectonic boundaries have been detected in the interior of the GHS, in the hanging wall of the Kakhtang thrust the detected pure-shear component is likely to be accommodated by a pervasive north–south transport-parallel lengthening (or stretching) of the GHS. At the orogen scale, the shear zones exposed in western Bhutan, which overprint the main fabric and displace the main fabric with a normal-sense motion, have the geometry of C′ shear bands (*sensu* Passchier & Trouw 1996) with respect to the margins of GHS. These ductile normal-sense shear zones also indicate a component of north–south transport-parallel lengthening of the

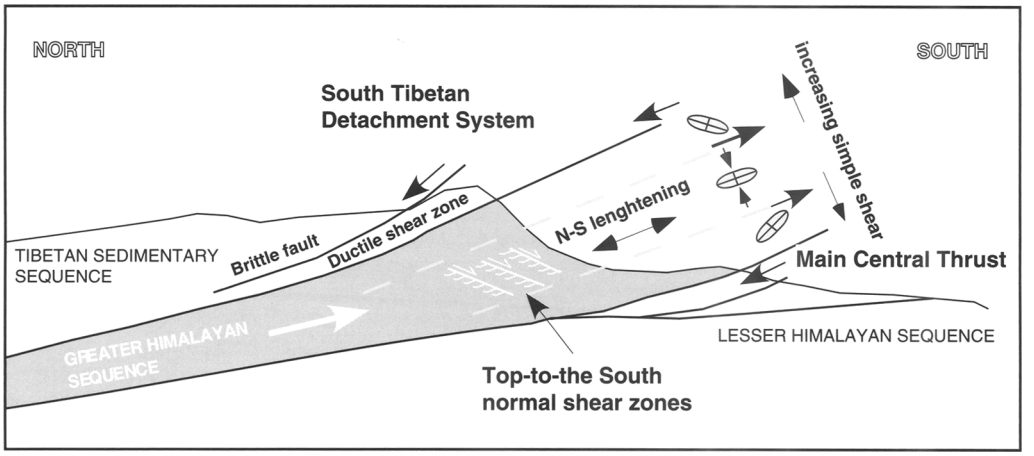

Fig. 11. Simplified sketch of inferred kinematics across the GHS, before development of out-of-sequence Kakhtang thrust, showing localization of the NSZ (20–17 Ma), and tentative schematic spatial distribution of vorticity values from the MCT up to the STDS during ductile extrusion at approximately 20–17 Ma. The interior of the GHS yields kinematic vorticity numbers implying an increasing component of pure shear deformation, whereas traced towards-the base (MCT; e.g. Grasemann *et al.* (1999) for NW India) and the top surface (STDS; e.g. Law *et al.* (2004) in the Everest massif) of the GHS deformation is dominated by simple shear, as suggested by extrusion models (Grujic *et al.* 1996, 2002; Grasemann *et al.* 1999).

GHS during exhumation (Fig. 9). Our geometric, kinematic and geochronological data support previously proposed models for ductile extrusion and exhumation of the GHS by Grasemann *et al.* (1999) and Grujic *et al.* (1996, 2002).

Conclusions

Structural and geochronological investigations of the interior of the GHS exposed in western Bhutan have revealed the presence of extensional shear zones, whose geometry, kinematics and age help to constrain the mode of extrusion and exhumation of the GHS. Moreover, they give further constraints on models widely adopted in many orogenic belts for extrusion of high-grade metamorphic cores. In particular the following points are noted.

1. The presence of ductile normal-sense motion shear zones (NSZ) cross-cutting the main penetrative fabric in the sillimanite-bearing gneisses, in the interior of the GHS, is documented.
2. The age of the NSZ has been bracketed at 20–17 Ma, i.e. during exhumation of the GHS, as previously proposed by Grujic *et al.* (2002) and Daniel *et al.* (2003).
3. Vorticity analysis points to an important component of pure shear acting contemporaneously with simple shear (*Wm* values bracketed between 0.63 and 0.76) both in the NSZ and in the surrounding gneisses.
4. Normal-sense motion on these shear zones indicates north–south transport-parallel lengthening of the upper central part of the GHS, accommodating the component of pure shear.
5. Comparison with available vorticity data along-strike in the Everest (Law *et al.* 2004) and Sutlej River (Grasemann *et al.* 1999) sections of the central and NW Himalaya, which were collected near the upper and lower tectonic boundaries of the extruding GHS respectively, and indicate an increase in the component of simple shear deformation, supports ductile extrusion models for the GHS proposed by Grujic *et al.* (1996, 2002) and Grasemann *et al.* (1999) in which vorticity of flow varies with structural position within the GHS.

Research was supported by funds from the University of Pisa and Istituto di Geoscienze e Georisorse, CNR Pisa (R. Carosi, C. Montomoli), PRIN Cofin 2003 (D. Visonà). C.M. wishes to thank Professor P. C. Pertusati for giving her the opportunity to encounter the spectacular Himalayan geology and for financial support. R.C., C.M. and D.V. wish to thank the guide Ugyen Tshering for helping them to cross the higher passes during heavy snowfalls on our 2003 expedition. D.R. would like to thank the Electron Microscopy Unit at The Australian National University for access to the SEM. We wish to thank C. Frassi for helping us with vorticity analysis measurements.

R. Law, D. Grujic and an anonymous referee are warmly acknowledged for constructive criticism.

References

ARITA, K. 1983. Origin of the inverted metamorphism of the Lower Himalayas. Central Nepal. *Tectonophysics*, **93**, 43–60.

AUDEN, J. B. 1935. Traverses in the Himalaya. *Records of the Geological Survey of India*, **69**, 123–141.

BEAUMONT, C., JAMIESON, R. A., NGUYEN, M. H. & LEE, B. 2001. Himalayan tectonics explained by extrusion of a low-viscosity channel coupled to focused surface denudation. *Nature*, **414**, 738–742.

BEAUMONT, C., JAMIESON, R. A., NGUYEN, M. H. & MEDVEDEV, S. 2004. Crustal channel flows: 1. Numerical models with applications to the tectonics of the Himalayan–Tibetan orogen. *Journal of Geophysical Research*, **109**, 1–29.

BLACK, L. P., KAMO, S. L., ALLEN, C. M., ALEINIKOFF, J. N., DAVIS, D. W., KORSCH, R. J. & FOUDOULIS, C. 2003. TEMORA 1: a new zircon standard for Phanerozoic U–Pb geochronology. *Chemical Geology*, **200**, 155–170.

BURCHFIEL, B. C., ZHILIANG, C., HODGES, K. V., YUPING, L., ROYDEN, L., CHANGRONG, D. & JIENE, X. 1992. *The South Tibetan Detachment System, Himalayan Orogen: extension contemporaneous with and parallel to shortening in a collisional mountain belt*. Geological Society of America Special Papers, **269**.

BURG, J. P., CHAUDRY, M. N., GAPAIS, D., CHEN, G. M. & LIU, G. H. 1984. Deformation of leucogranites of the crystalline main central thrust sheet in southern Tibet (China). *Journal of Structural Geology*, **6**, 535–542.

BUTERA, K., WILLIAMS, I., BLEVIN, P. & SIMPSON, C. 2001. Zircon U–Pb dating of Early Palaeozoic monzonitic intrusives from the Goonumbla area, New South Wales. *Australian Journal of Earth Science*, **48**, 457–464.

CABY, R., PÊCHER, A. & LE FORT, P. 1983. Le grand chevauchement central himalayen: nouvelles données sur le métamorphisme inverse à la base de la Dalle du Tibet. *Revue Géologie Dynamique Géographie Physique*, **24**, 89–100.

CABY, R., HAMMOR, D. & DELOR, C. 2001. Metamorphic evolution, partial melting and Miocene exhumation of lower crust in the Edough metamorphic core complex, west Mediterranean orogen, eastern Algeria. *Tectonophysics*, **342**, 239–273.

CAROSI, R., LOMBARDO, B., MUSUMECI, G. & PERTUSATI, P. C. 1999. Geology of the Higher Himalayan Crystallines in Khumbu Himal (Eastern Nepal). *Journal of Asian Earth Sciences*, **17**, 785–803.

CASTELLI, D. & LOMBARDO, B. 1983. The Gophu La and Western Lunana granites: Miocene muscovite leucogranites of the Bhutan Himalaya. *Lithos*, **21**, 211–225.

CHEMENDA, A. I., MATTAUER, M., MALAVIEILLE, J. & BOKUN, A. N. 1995. A mechanism for syncollisional rock exhumation and associated normal faulting: Results from physical modelling. *Earth and Planetary Science Letters*, **132**, 225–232.

CHEMENDA, A. I., MATTE, P. & SOKOLOV, V. 1997. A model of Palaeozoic obduction and exhumation of high-pressure/low-temperature rocks in the southern Urals. *Tectonophysics*, **276**, 217–227.

CHEMENDA, A. I., BURG, J.-P. & MATTAUER, M. 2000. Evolutionary model of the Himalaya–Tibet system: geopeom based on new modeling and geophysical data. *Earth and Planetary Science Letters*, **174**, 397–409.

COMPSTON, W., WILLIAMS, I. S. & MEYER, C. 1984. U–Pb geochronology of zircons from lunar breccia 73217 using a sensitive high mass-resolution ion microprobe. *Journal of Geophysical Research*, **89**, B525–B534.

DANIEL, C. G., HOLLISTER, L. S., PARRISH, R. R. & GRUJIC, D. 2003. Exhumation of the Main Central Thrust from lower crustal depths, Eastern Bhutan Himalaya. *Journal of Metamorphic Geology*, **21**, 317–334.

DAVIDSON, C., GRUJIC, D. E., HOLLISTER, L. S. & SCHMID, S. M. 1997. Metamorphic reactions related to decompression and synkinematic intrusion of leucogranite, High Himalayan Crystallines, Bhutan. *Journal of Metamorphic Geology*, **15**, 593–612.

DIETRICH, V. & GANSSER, A. 1981. The leucogranites of the Bhutan Himalaya (crustal anatexis versus mantle melting). *Schweizerische Mineralogische und Petrographische Mitteilungen*, **61**, 177–202.

ECHTLER, H. P., IVANOV, K. S., RONKIN, Y. L., KARSTEN, L. A., HETZEL, R. & NOSKOV, A. G. 1997. The tectono-metamorphic evolution of gneiss complexes in the Middle Urals, Russia: reappraisal. *Tectonophysics*, **276**, 229–251.

EDWARDS, M. A. & HARRISON, T. M. 1997. When did the roof collapse? Late Miocene N–S extension in the High Himalaya revealed by Th-Pb monazite dating of the Khula-Kangri granite. *Geology*, **25**, 543–546.

EDWARDS, M. A., KIDD, W. S. F., LI, J., YUE, Y. & CLARK, M. 1996. Multi-stage development of the southern Tibet detachment system near Khula Kangri: New data from Gonta La. *Tectonophysics*, **260**, 1–19.

EDWARDS, M. A., PECHER, A., KIDD, W. S. F., BURCHFIEL, B. C. & ROYDEN, L. H. 1999. Southern Tibetan Detachment System at Khula Kangri, eastern Himalaya: a large-area, shallow detachment stretching into Bhutan? *Journal of Geology*, **107**, 623–311.

FAURE, M., LIN, W., SCHÄRER, U., SHU, L., SUN, Y. & ARNAUD, N. 2003. Continental subduction and exhumation of UHP rocks. Structural and geochronological insights from Dabieshan (East Chian). *Lithos*, **70**, 213–241.

FERRARA, G., LOMBARDO, B., TONARINI, S. & TURI, B. 1991. Sr, Nd and O isotopic characterization of the Gophu La and Gumburanjun leucogranites (High Himalaya). *Schweitzerische Mineralogische Petrographische Mitteilungen*, **71**, 35–51.

GANSSER, A. 1964. *Geology of the Himalaya*. Wiley-Interscience, London.

GANSSER, A. 1983. *Geology of the Bhutan Himalaya*. Denkschriften der Schweizerischen Naturforschenden Gesellschaft, **96**, Birkhäuser Verlag, Basel.

GRASEMANN, B., FRITZ, H. & VANNAY, J. C. 1999. Quantitative kinematic flow analysis from the Main Central Thrust Zone (NW-Himalaya, India); implications for a decelerating strain path and the extrusion of orogenic wedges. *Journal of Structural Geology*, **21**, 837–853.

GRAY, D. R., MILLER, J. MCL., FOSTER, D. A. & GREGORY, R. T. 2004. Transition from subduction-to exhumation-related fabrics in glaucophane-bearing eclogites, Oman: evidence from relative fabric chronology and $^{40}Ar/^{39}Ar$ ages. *Tectonophysics*, **389**, 35–64.

GRUJIC, D., CASEY, M., DAVIDSON, C., HOLLISTER, L., KUNDIG, K., PAVLIS, T. & SCHMID, S. 1996. Ductile extrusion of the Higher Himalayan crystalline in Bhutan: evidence from quartz microfabrics. *Tectonophysics*, **260**, 21–43.

GRUJIC, D., HOLLISTER, L. & PARRISH, R. R. 2002. Himalayan metamorphic sequence as an orogenic channel: insight from Bhutan. *Earth and Planetary Science Letters*, **198**, 177–191.

HEIM, A. & GANSSER, A. 1939. *Central Himalaya. Geological observations of the Swiss Expedition 1936*. Mémoires de la Société Helvétique des Sciences Naturelles **73/1**.

HERREN. E. 1987. Zanskar shear zone: northeast-southwest extension within the Higher Himalayas (Ladakh, India). *Geology*, **15**, 145–160.

HODGES, K. V. 2000. Tectonics of the Himalaya and southern Tibet from two perspectives. *Geological Society of America Bullettin*, **112**, 324–350.

HODGES, K. V., PARRISH, R. R., HOUSCH, T. B., LUX, D. R., BURCHFIEL, B. C., ROYDEN, L. H. & CHEN, Z. 1992. Simultaneous Miocene extension and shortening in the Himalayan orogen. *Science*, **258**, 1466–1479.

HOSKIN, P. W. O. & SCHALTEGGER, U. 2003. The composition of zircon and igneous and metamorphic petrogenesis. *In*: HANCHAR, J. M. & HOSKIN, P. W. O. (eds) *Zircon*. Mineralogical Society of America, Washington, 27–62.

HUDLESTON, P. 1999. Strain compatibility and shear zones: is there a problem? *Journal of Structural Geology*, **21**, 923–932.

JAMIESON, R. A., BEAUMONT, C., MEDVEDEV, S. & NGUYEN, M. H. 2004. Crustal channel flows: 2. Numerical models with implications for metamorphism in the Himalayan-Tibetan orogen. *Journal of Geophysical Research*, **109**, 1–24.

JESSUP, M. J., LAW, R. D., SEARLE, M. P. & HUBBARD, M. S. 2006. Structural evolution and vorticity of flow during extrusion and exhumation of the Greater Himalayan Slab, Mount Everest Massif, Tibet/Nepal: implications for orogen-scale flow partitioning. *In*: LAW, R. D., SEARLE, M. P. & GODIN, L. (eds) *Channel Flow, Ductile Extrusion and Exhumation in Continental Collision Zones*. Geological Society, London, Special Publication, **268**, 379–413.

LAW, R. D., SEARLE, M. P. & SIMPSON, R. L. 2004. Strain, deformation temperatures and vorticity of flow at the top of the Greater Himalyan Slab, Everest Massif, Tibet. *Journal of the Geological Society, London*, **161**, 305–320.

LE FORT, P. 1975. Himalyas: the collided range. Present knowledge of the continental arc. *American Journal of Science*, **275-A**, 1–44.

LUDWIG, K. R. 2000. *Isoplot/Ex version 2.4. A geochronological toolkit for Microsoft Excel*. Berkeley Geochronological Centre, Special Publication, **56**.

NELSON, K. D., ZHAO, W., BROWN, L. D. *ET AL.* 1996. Partially molten middle-crust beneath southern Tibet: synthesis of project INDEPTH results. *Science*, **274**, 1684–1688.

PASSCHIER, C. W. 1987. Stable position of rigid objects in non-coaxial flow – a study in vorticity analysis. *Journal of Structural Geology*, **9**, 679–690.

PASSCHIER, C. W. & TROUW, R. A. J. 1996. *Microtectonics*. Springer-Berlag, Berlin.

RAMSAY, J. G. 1980. Shear zone geometry: a review. *Journal of Structural Geology*, **2**, 83–99.

RAMSAY, J. G. & HUBER, I. M. 1987. *The Techniques of Modern Structural Geology, Vol. 2: Folds and Fractures*. Academic Press, London.

ROWLEY, D. B. 1988. Minimum age of initiation of collision between India and Asia north of Everest based on subsidence history of Zhepure mountain section. *Journal of Geology*, **106**, 229–235.

RUBATTO, D. & GEBAUER, D. 2000. Use of cathodoluminescence for U–Pb zircon dating by ion microprobe: some examples from the Western Alps. *In*: PAGEL, M., BARBIN, V., BLANC, P. & OHNENSTETTER, D. (eds) *Cathodoluminescence in Geosciences*. Springer, Berlin, 373–400.

SEARLE, M. P., WINDLEY, B. F., COWARD, M. P. *ET AL.* 1987. The closing of Tethys and tectonics of the Himalaya. *Geological Society of America Bulletin*, **98**, 678–701.

SEARLE, M. P., COOPER, D. J. W. & REX, A. J. 1988. Collision tectonics of the Ladakh-Zanskar Himalaya. *Philosophical Transactions of the Royal Society, London*, **A326**, 117–150.

SEARLE, M. P., WARREN, C. J., WATERS, D. J. & PARRISH, R. R. 2004. Structural evolution, metamorphism and restoration of the Arabian continental margin, Saih Hatat region, Oman Mountains. *Journal of Structural Geology*, **26**, 451–473.

SIMPSON, C. & DE PAOR, D. 1993. Strain and kinematic analysis in general shear zones. *Journal of Structural Geology*, **15**, 1–20.

SWAPP, S. M. & HOLLISTER, L. S. 1991. Inverted metamorphism within the Tibetan slab of Bhutan: evidence for a tectonically transported heat-source. *Canadian Mineralogist*, **29**, 1019–1041.

VANNAY, J.-C. & GRASEMANN, B. 2001. Himalayan inverted metamorphism and syn-convergence extension as a consequence of a general shear extrusion. *Geological Magazine*, **138**, 253–276.

VISONÀ, D. & LOMBARDO, B. 2002. Two mica- and tourmaline leucogranites from the Everest-Makalu region (Nepal-Tibet). Himalayan leucogranite genesis by isobaric heating? *Lithos*, **62**(3-4), 125–150.

WALLIS, R. S. 1992. Vorticity analysis in a metachert from the Sanbagawa Belt, SW Japan. *Journal of Structural Geology*, **14**, 271–280.

WALLIS, R. S. 1995. Vorticity analysis and recognition of ductile extension in the Sanbagawa Belt, SW Japan. *Journal of Structural Geology*, **17**, 1077–1093.

WALLIS, R. S., PLATT, J. P. & KNOTT, S. D. 1993. Recognition of syn-convergence extension in accretionary wedges with examples from the Calabrian arc and the Eastern Alps. *American Journal of Science*, **293**, 463–495.

WIESAMAYR, G., EDWARDS, M. A., MEYER, M., KIDD, W. S. F., LEBER, D., HÄUSLER, H. & WANGDA, D. 2002. Evidence for steady fault-accommodated strain in the High Himalaya: progressive fault rotation of the southern Tibet detachment system in NW Bhutan. *In*: DE MEER, S., DRURY, M. R., DE BRESSER, J. H. P. & PENNOK, G. M. (eds) *Deformation Mechanisms, Rheology and Tectonics: Current Status and Future Perspectives*. Geological Society, London, Special Publications, **200**, 371–386.

WILLIAMS, I. S., BUICK, I. S. & CARTWRIGHT, I. 1996. An extended episode of early Mesoproterozoic metamorphic fluid flow in the Reynolds Range, central Australia. *Journal of Metamorphic Geology*, **14**, 29–47.

XYPOLIAS, P. & KOUKOUVELAS, I. K. 2001. Kinematic vorticity and strain rate patterns with ductile extrusion in the Chemos Shear Zone (External Hellenides, Greece). *Tectonophysics*, **338**, 59–77.